An Advanced Closed-Loop Control to Improve the Performance of Hybrid Stepper Motors

Kien Minh Le, Hung Van Hoang, and Jae Wook Jeon, *Member, IEEE*

Abstract—This paper presents an effective closed-loop control approach for a stepper motor. The proposed approach consists of motor parameter identification, closed-loop current control, closed-loop position control, and damping control. The presented implementation achieves accurate position, high torque, and smooth speed. By using an improved proportional-integral current control algorithm, this approach not only guarantees the current tracking performance but also increases the bandwidth during the speed response. The advanced position controller achieves both high torque and the synchronous condition of the motor after a loss of synchronism occurs. In addition, this method applies an effective speed damping method to remove resonance at low speed and reduce vibration at high speed. All the proposed algorithms were implemented on an industrial test-bench. The experimental results demonstrate the validity of the proposed approach for practical applications.

Index Terms—Damping, phase advance control, proportional-integral (PI) controller, stepper motor, step-out.

I. INTRODUCTION

STEPPER motors are widely used in commercial and industrial applications such as robotic systems, CNC machines, printers, and domestic appliances [1]. The requirements of a stepper motor drive are fast acceleration, smooth speed, accurate position, and high torque.

Stepper motors can generally be operated in open-loop mode or closed-loop mode, and they have been heavily studied. In open-loop mode, controlling the currents in the coils of the motor is the heart of the control in stepper motor drives. Various effective control schemes, such as conventional proportional-integral (PI) control [2], intelligent control [3], and fuzzy control [4], have been investigated for closed-loop current control. However, in these schemes, the current controller coefficients are determined based only on the motor parameters, or the computations are complex. In this paper, an advanced PI current controller is proposed whose coefficients are calculated based on the motor parameters and the operating speed.

K. M. Le and J. W. Jeon are with the School of Information and Communication Engineering, Sungkyunkwan University, Suwon 440-746, South Korea (e-mail: kienha@skku.edu; jwjeon@yurim.skku.ac.kr).

H. V. Hoang is with the Fastech Company Ltd., Gyeonggi 440-746, South Korea (e-mail: hunghv2012@gmail.com).

Open-loop drives are low cost and have simple control algorithms because they do not require an additional position sensor. However, a problem of this scheme is step-out when the load torque varies, especially at high speeds, and this problem can occur from even a small torque disturbance.

The step-out can be avoided by using a closed-loop control algorithm. Various control methods based on phase advance control have been studied for closed-loop drives [5]–[7]. In these, the phase advance angle was calculated considering the produced torque, the motor speed, and compensation for the back electromotive force (EMF) [7]. Using this method, the motor can be operated at high speed with high-produced torque. However, this method requires complex computations. Furthermore, closed-loop drives with phase advance control are very effective for avoiding step-out in low-speed range. At high speeds, if a loss of synchronism occurs, the motor may not follow the command, or a large overshoot may be produced. This leads to nonguaranteed position and speed tracking performances. In this paper, we propose an advanced closed-loop position control method based on phase advance control to overcome this problem.

For a stepper motor to operate perfectly over its full speed range, an important problem is how to avoid or overcome resonance at low speeds and vibration at high speeds. Several schemes using microstepping or combining of microstepping with a closed loop have been discussed in [8]–[10]. These approaches have improved speed performance. However, they are effective at either low speeds [8] or medium and high speeds [10], but not over all speeds. To improve the speed performance of stepper motor drives, many damping algorithms using nonlinear control have been applied, such as the Kalman filter, adaptive approach, sliding mode control technique, model-based control, Jacobian linearization observer, harmonic injection scheme, and optimal control [5], [11]–[19]. These schemes effectively eliminate torque ripples caused by the nonlinear characteristics of the stepper motor. Moreover, intelligent control algorithms have been used to damp out the resonance and vibration of the stepper motor, including genetic algorithms [20], learning schemes [21], fuzzy logic algorithms [22], and artificial neural network techniques [23]. These methods improve the stability in transient dynamics and the tracking characteristics during the speed response by reducing torque ripples and disturbances. However, these nonlinear control and intelligent control approaches normally require complex calculations and a high computing load. In addition, they do not work effectively over the whole speed range. In this paper, we propose an effective damping control method to smooth the motor speed over the full speed range.

Nowadays, many sensor-less control techniques of permanent magnet synchronous motors have been developed for industrial drives. Generally, sensor-less control methods to estimate the position of the motor shaft are commonly based on either the back EMF for medium- and high-speed applications or the high-frequency pulse injection for low-speed applications [24]. Most of the sensor-less estimation methods for stepper motors were based on the back-EMF effect because the high-frequency pulse injection method is complicated for control applications [25]. Furthermore, in comparison to other kinds of motors, the stepper motor has a special torque specification that is high at low speed and low at high speed. Therefore, most applications use stepper motors in the low-speed range to achieve good characteristics and high positional accuracy. Since a sensor-less control approach is not reliable enough to apply for industrial applications using stepper motors, a mechanical sensor is applied for the stepper motor control system in this study.

The main contributions of this paper are as follows.

1) We propose a new model for stepper motor analysis based on the cogging torque and the torque caused by the reluctance effect. This model clearly represents the oscillation characteristics of the stepper motor in the low frequency domain.

2) We provide an improved current control scheme based on a conventional PI algorithm to adapt to changes of motor parameters and operating speed. This scheme increases the operating bandwidth of the stepper motor.

3) We propose an advanced position control method to obtain high produced torque and recover the speed when a loss of synchronism occurs.

4) We provide an effective method for damping speed to eliminate motor resonance and vibration. This enables the stepper motor to operate smoothly over full operating speed range.

5) Finally, we conduct an experiment using a digital signal processor (DSP)-based stepping motor drive platform used for industrial applications to verify the effectiveness of the proposed approach.

The rest of this paper is organized as follows. The proposed dynamic model is introduced briefly in Section II. The proposed identification technique is described in Section III. Section IV explains the design of the proposed current controller. The position control loop is introduced in Section V. Section VI describes how to perform the proposed speed damping method. Section VII presents the implementation and experimental results verifying the proposed approach. Finally, the conclusions are summarized in Section VIII.

II. STEPPER MOTOR MODEL

A two-phase bipolar hybrid stepper motor is considered in this research, with electrical equations given by Lee *et al.* [9]

$$L\frac{di_a}{dt} = v_a - Ri_a + K_t\omega\sin\theta$$

$$L\frac{di_b}{dt} = v_b - Ri_b - K_t\omega\cos\theta. \quad (1)$$

TABLE I
VARIABLE AND PARAMETER DEFINITIONS

Variable	Description	Unit
v_a, v_b	Phase Voltages	V
i_a, i_b	Phase Currents	A
ω	Mechanical Speed of Rotor Shaft	rad/s
θ	Electrical Position of Rotor	rad

Parameter	Description	Unit
R	Resistance	Ω
L	Inductance	H
K_t	Torque Constant	$N \cdot m/A$
J	Rotor Inertia	$N \cdot m \cdot s^2/rad$
D	Damping Coefficient	$N \cdot m \cdot s/rad$
T_L	Load Torque	$N \cdot m$
K_{dj}	Amplitude of jth harmonic	$N \cdot m$
ϕ_j	Phase Shift of jth harmonic	rad

Generally, the motor torque consists of three different components: an electrodynamic component (T_E), a cogging torque component (T_C), and a component (T_R) created by the reluctance effect [1]. T_E is caused by the interaction between the stator currents and the permanent magnet rotor field, and it is dominant

$$T_E = -K_t i_a\sin\theta + K_t i_b\cos\theta. \quad (2)$$

T_C is caused by the multitoothed construction and predicted as follows [26]:

$$T_C = -\sum_{j=1}^{\infty} K_{dj}\sin(4j\theta) \quad (3)$$

where j is a positive integer and K_{dj} is the amplitude of the jth harmonic.

Here, T_R is generally very small in stepper motors, so it can be ignored.

However, in this paper, both T_C and T_R are proposed to produce harmonics with various frequencies

$$T_C + T_R = -\sum_{j=1}^{\infty} K_{dj}\sin(j\theta + \phi_j) \quad (4)$$

where ϕ_j is the initial phase of the jth harmonic.

Finally, the equations of motion are given by [8]

$$J\frac{d\omega}{dt} = (-K_t i_a\sin\theta + K_t i_b\cos\theta) - \sum_{j=1}^{\infty} K_{dj}\sin(j\theta + \phi_j)$$

$$- D\omega - T_L \quad (5)$$

$$\frac{d\theta}{dt} = N_r\omega. \quad (6)$$

All variables and parameters are listed in Table I.

III. MOTOR PARAMETER IDENTIFICATION

In this study, a simple and effective technique is proposed to identify two motor parameters, the resistance R and inductance L, in the standstill condition. Because each phase of the motor is considered as an *RL*-circuit, the parameters identification is
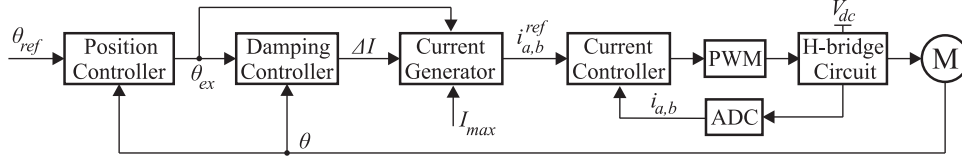
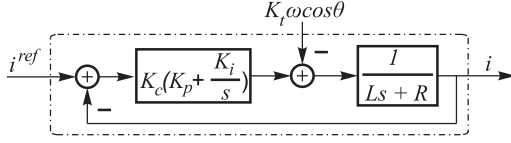Fig. 1.   Block diagram of the proposed stepper motor control system.

Fig. 2.   Block diagram of current control loop.

based on the current step response, which is given as

$$i(t) = \frac{U_0}{R}\left(1 - e^{-\frac{R}{L}t}\right) = I_{\max}\left(1 - e^{-\frac{R}{L}t}\right) \quad (7)$$

where U_0 is the amplitude of the commanded step voltage, and $I_{\max} = \frac{U_0}{R}$. The current step response is divided into two separate parts for the transient and steady-state regions.

In the steady-state region, the resistance R is obtained as

$$R = \frac{U_0}{I_{\max}}. \quad (8)$$

In the transient region, I_T is the measured current at a given time T, and then the inductance L is approximately derived based on (7) as follows:

$$L \approx \frac{TR}{\frac{I_T}{I_{\max}} + \left(\frac{I_T}{I_{\max}}\right)^2 + \left(\frac{I_T}{I_{\max}}\right)^3}. \quad (9)$$

This identification scheme is performed to solve two problems in the control of stepper motors in real applications, as follows:

1) *Solution 1:* When connecting an unidentified motor, the drive can work well without the input of the motor parameters.
2) *Solution 2:* When the stepper motor system is operated in different environments, such as under a high temperature or high magnetic field, the motor parameters change. The proposed method can easily solve this problem by restarting the system to reidentify the motor parameters to always ensure optimal control for that system.

IV. CURRENT CONTROL LOOP

The electrical equations in (1) are considered to design the current controller for the stepper motor, and the designs of current control for both phases of the motor are the same. Fig. 2 shows the current control loop of phase B of the motor. The improved PI current controller is proposed as

$$PI(s) = K_c\left(K_p + \frac{K_i}{s}\right). \quad (10)$$

Compared to the conventional PI control algorithm, the proposed improved PI current controller has one more gain called the speed compensation gain K_c. In this study, both gains K_p and K_i depend on the motor parameters (R and L), whereas the gain K_c is determined by the motor operating speed. Therefore, the improved PI current controller adapts to changes of motor parameters and operating speed.

By using a zero cancellation technique and comparing the closed-loop characteristic polynomial of the current control loop shown in Fig. 2 to the standard second-order system with damping ratio ξ and natural frequency ω_0, we obtain the coefficients of the proposed improved PI current controller as

$$K_p = \frac{2\xi\omega_0 L - R}{K_c} \quad \text{and} \quad K_i = \frac{\omega_0^2 L}{K_c}. \quad (11)$$

It should be noted that ω_0 determines the bandwidth of the current loop. On the other hand, for stepper motors using microstepping algorithm, the motor operating speed is directly related to the excitation frequency of the reference current. Therefore, in order to enlarge the bandwidth of the motor operating speed the bandwidth of the current loop needs to be increased. From (11), the gain K_c is changed following the operating speed to maintain the current performance. In general, the speed of most stepper motors is in a range of [0:5 00 000 pulses per second (pps)] (equivalent to [0:3000 r/min]). Through our experience in this study, K_c is selected in the range [1:12] and given by

$$K_c = \frac{11}{5\,00\,000}\omega + 1. \quad (12)$$

At low speed, the current controller does not require high gain to reduce the motor vibration and noise. Otherwise, the controller requires a high enough gain to follow the current command at high speed. Our proposed scheme effectively satisfies these requirements.

The back EMF feature of the motor is also an important term. Especially in the high-speed range, the current in the coil is reduced because of the large back EMF, and the motor torque is therefore reduced. It is not easy to eliminate the back EMF. However, the proposed current controller improves the motor performance over a large operating speed range.

V. POSITION CONTROL LOOP

In previous phase advance control methods, by determining an appropriate phase excitation scheme, the motor can be operated in the closed-loop control mode with the highest torque, even with a variable load [5]–[7]. In addition, because these methods only consider the feedback position, the motor operates well at low speed or when the position error between the reference and feedback positions is small (the loss of
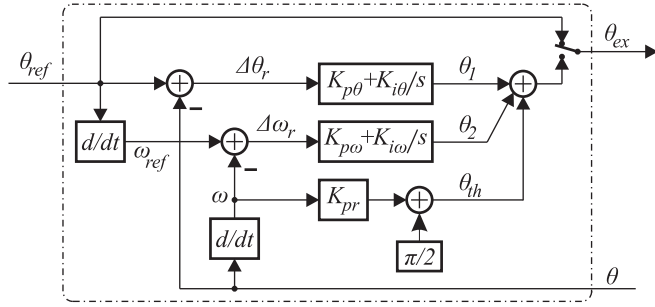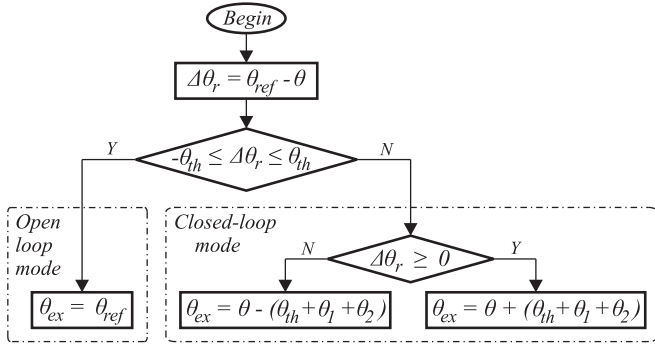
Fig. 3. Block diagram of position control loop.

Fig. 4. Position control loop algorithm.

Fig. 5. Block diagram of damping control.

synchronism occurs during only a short time). Furthermore, there is vibration when the motor is stopped.

To overcome all these problems, we propose an advanced position control method in this study. This method is shown in Fig. 3 and is based on phase advance control considering not only the feedback position, but also the position error and the speed error between the reference and feedback speeds. The control law is shown in Fig. 4. The position controller is operated in either open-loop mode or closed-loop mode, depending on the comparison value between the position error $\Delta\theta_r$ and the threshold value θ_{th} given in (13).

$$\theta_{th} = K_{pr}\omega + \pi/2. \qquad (13)$$

In open-loop mode, the phase excitation angle θ_{ex} is similar to the reference position θ_{ref}. However, in closed-loop mode, two PI controllers are used to adjust the phase excitation angle. These two controllers are described in (14) and (15) and are used to eliminate the position error and the speed error, respectively,

$$PI_\theta(s) = K_{p\theta} + \frac{K_{i\theta}}{s} \qquad (14)$$

$$PI_\omega(s) = K_{p\omega} + \frac{K_{i\omega}}{s}. \qquad (15)$$

In Fig. 3, when the synchronism is lost, the position error $\Delta\theta_r$ is increased, and the output θ_1 of the upper PI controller is correspondingly increased. This leads to an increase in the phase excitation angle θ_{ex}, and the motor speed ω is therefore increased. During this time, the position error has a very large value, so θ_1 dominates. The motor is operated at a high speed until the position error becomes small, and the θ_1 term is reduced
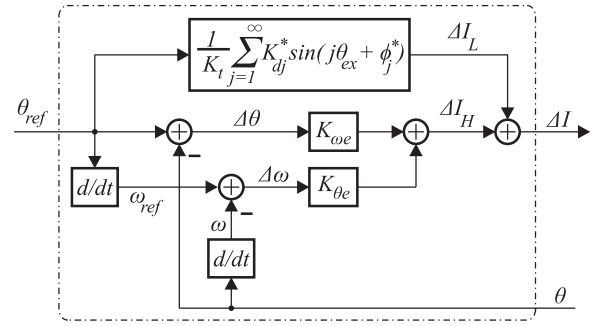
to as small as possible due to the integral term of the PI controller. Finally, the motor speed tracks the reference speed. The same explanation applies to the lower PI controller for the speed error. The proposed method achieves speed recovery when a loss of synchronism occurs and reduces vibration when the motor is stopped. The experimental results provided later demonstrate the effectiveness of this method.

VI. DAMPING METHOD

The proposed control law is almost the same as that described in [8], but the actual electrical position θ is replaced by the reference electrical position θ_{ref} (or θ_{ex} in the closed-loop position control mode), as follows:

$$i_a = I_{max}\cos(\theta_{ref}) - \Delta I\sin(\theta_{ref})$$
$$i_b = I_{max}\sin(\theta_{ref}) + \Delta I\cos(\theta_{ref}) \qquad (16)$$

where I_{max} is the microstepping gain, and ΔI is a compensation function.

The proposed current compensation algorithm above consists of two separate parts. The first terms on the right hand side of (16) are reference current parts that are exactly the same traditionally sinusoidal signals used for microstepping the stepper motor. The second terms are compensation current parts that are fundamental for performing the damping method introduced below.

A block diagram illustrating the proposed damping method is shown in Fig. 5. The compensation function ΔI, which is controlled to remove resonance in the low-speed range and to reduce vibration in the high-speed range, is divided into two separate components, as follows:

$$\Delta I = \Delta I_L + \Delta I_H \qquad (17)$$

where ΔI_L and ΔI_H are low- and high-speed compensation functions for damping at low speed and high speed, respectively.

Substituting (16) and (17) into (5), a resulting equation of motion considering low- and high-speed compensation functions is obtained

$$J\dot\omega + D\omega + T_L = (K_t I_{max}\sin\Delta\theta + K_t\Delta I_H\cos\Delta\theta)$$
$$+ \left(K_t\Delta I_L\cos\Delta\theta - \sum_{j=1}^{\infty} K_{dj}\sin(j\theta + \phi_j)\right). \qquad (18)$$

This study shows the two following important features:
1) *Feature 1:* In the low-speed range, ΔI_L is dominant and strongly removes the resonances caused mainly by the cogging torque and the reluctance torque. Hence, in this speed range, (17) becomes $\Delta I \approx \Delta I_L$.
2) *Feature 2:* In contrast, in the high-speed range, the motor quickly accelerates over the resonance region, so ΔI_H dominates and effectively reduces the vibration, and (17) becomes $\Delta I \approx \Delta I_H$.

A. In Low-Speed Range

In the low-speed range, the resonance problem is natural and always occurs with all stepper motors [27]. In this study, ΔI_L is used to remove all resonances, and (18) now becomes

$$J\dot{\omega} + D\omega + T_L = K_t I_{\max}\sin\Delta\theta$$
$$+ \left(K_t \Delta I_L \cos\Delta\theta - \sum_{j=1}^{\infty} K_{\mathrm{dj}}\sin(j\theta + \phi_j)\right). \quad (19)$$

The damping procedure involves two steps, as follows:

Step 1: The motor is accelerated to a consistent speed to clearly observe all resonances. Next, all the harmonics in (4) are identified at the corresponding resonant frequencies at which the speed error oscillates strongly. Specifically, only the amplitude K_{dj} is determined according to (20), obtained from an approximation of (5), while the phase shift ϕ_j is assumed to be zero

$$K_{\mathrm{dj}} \approx D\Delta\omega_j \quad (20)$$

where $\Delta\omega_j$ is the speed error corresponding to the jth harmonic.

Step 2: ΔI_L is given by

$$\Delta I_L = \frac{1}{K_t}\sum_{j=1}^{\infty} K_{\mathrm{dj}}^*\sin(j\theta_{\mathrm{ref}} + \phi_j^*) \quad (21)$$

where K_{dj}^* and ϕ_j^* are the amplitude and the phase shift of the jth-harmonic compensation function, respectively. Each harmonic in (21) is used to remove one corresponding harmonic expressed via the last term on the right hand side of (19). Both parameters (K_{dj}^* and ϕ_j^*) are found and optimized by the integral of absolute error (IAE)

$$\mathrm{IAE}_j = \int_0^{\infty} |\Delta\omega_j|dt \to \min. \quad (22)$$

Specifically, for each jth harmonic, the procedure of optimizing K_{dj}^* and ϕ_j^* is performed as follows:
1) First, the motor is operated with K_{dj} obtained in Step 1 ($K_{\mathrm{dj}}^* = K_{\mathrm{dj}}$), and ϕ_j^* is varied from 0 to 2π rad. The optimal phase shift ϕ_j^* is obtained through (22).
2) Next, operating the motor with the optimal value ϕ_j^* obtained above, K_{dj}^* is varied within the range of $[K_{\mathrm{dj}\min}^*, K_{\mathrm{dj}\max}^*]$ determined by the requirement that $|\Delta\theta| < \pi/2$, in order to avoid step-out. After using (22), the optimal amplitude K_{dj}^* is acquired.

B. In High-Speed Range

In the high-speed range, the most important objective is to reduce the vibration of the stepper motor.

The high-speed compensation function is given by

$$\Delta I_H = K_\omega \Delta\omega + K_\theta \Delta\theta \quad (23)$$

where $\Delta\omega$ and $\Delta\theta$ are speed and position errors, respectively,

$$\Delta\omega = \omega_{\mathrm{ref}} - \omega \quad (24)$$

$$\Delta\theta = \theta_{\mathrm{ref}} - \theta. \quad (25)$$

where K_ω and K_θ are speed and position gains, respectively. Both are used to regulate the speed and position errors via modulation of Δ_H. The dynamic response of the system is shaped by the choice of gain values, K_ω and K_θ.

Substituting (23)−(25) into (18), we obtain

$$J\dot{\omega} + D\omega + T_L = K_t I_{\max}\sin\Delta\theta$$
$$+ K_t\cos\Delta\theta[K_\omega\Delta\omega + K_\theta\Delta\theta]. \quad (26)$$

From (24) and (25), we have

$$\Delta\dot{\omega} = \dot{\omega}_{\mathrm{ref}} - \dot{\omega} \quad (27)$$

$$\Delta\dot{\theta} = N_r\Delta\omega. \quad (28)$$

Taking the derivative of both sides of (26), assuming T_L is constant (i.e., $\dot{T}_L = 0$), and combining this with (28), we have

$$J\ddot{\omega} + D\dot{\omega} = [(I_{\max} + K_\theta)K_t N_r\cos\Delta\theta]\Delta\omega$$
$$+ (K_t K_\omega\cos\Delta\theta)\Delta\dot{\omega} - K_t N_r\sin\Delta\theta[K_\omega\Delta\omega^2 + K_\theta\Delta\omega\Delta\theta]. \quad (29)$$

Because $\Delta\omega$ and $\Delta\theta$ are small, $\Delta\omega^2$ and $\Delta\omega\Delta\theta$ are also small. Combining this with (27), and noticing that, at steady state, $\dot{\omega}_{\mathrm{ref}} = 0$ because $\omega_{\mathrm{ref}} = \mathrm{const}$, the transfer function of the motor speed is

$$\frac{\omega}{\omega_{\mathrm{ref}}} =$$
$$\frac{(I_{\max} + K_\theta)K_t N_r\cos\Delta\theta}{Js^2 + (D + K_t K_\omega)\cos\Delta\theta)s + (I_{\max} + K_\theta)K_t N_r\cos\Delta\theta}. \quad (30)$$

Comparing (30) to the standard second-order system, which has a natural frequency (ω_0) and a damping ratio (ξ), we obtain

$$K_\omega = \frac{2\xi\omega_0 J - D}{K_t\cos\Delta\theta} \quad (31)$$

$$K_\theta = \frac{\omega_0^2 J}{N_r K_t\cos\Delta\theta - I_{\max}}. \quad (32)$$

To determine the two coefficients (K_ω and K_θ), unless both ω_0 and ξ are easily obtained from the desired performance requirement, it is also necessary to know $\Delta\theta$.

At steady state, $\Delta I \approx 0$, $\omega \approx \omega_{\mathrm{ref}}$, and $\dot{\omega} \approx 0$. Consequently, an approximation is applied to (26) to obtain

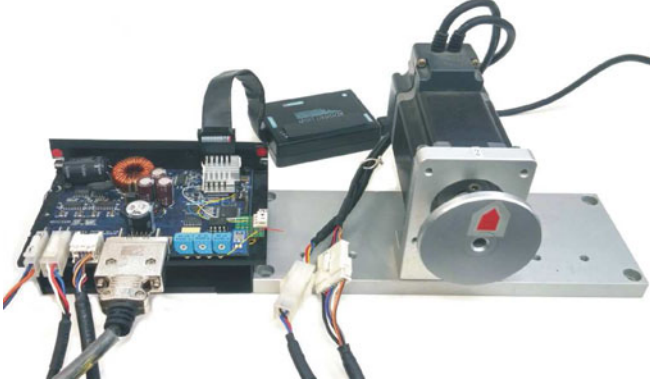$$D\omega_{\mathrm{ref}} + T_L = K_t I_{\max}\sin\Delta\theta. \quad (33)$$

Fig. 6.   Experimental system.

TABLE II
EzM-56L MOTOR PARAMETERS

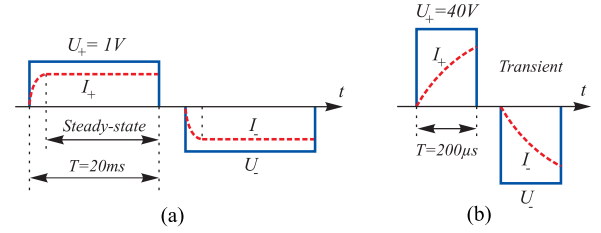| Parameter	Value
Phase Resistance (R)	2.3 Ω
Phase Inductance (L)	7.35 mH
Torque Constant (K_t)	0.83 N $\cdot$ m/A
Rotor Inertia (J)	0.0000269 N $\cdot$ m $\cdot$ s^2/rad
Damping Coefficient (D)	0.0013 N $\cdot$ m $\cdot$ s/rad
Load Torque (T_L)	0.029 N $\cdot$ m
Number of Poles (N_r)	50
Source Voltage (V)	40 V
Current Rate (I)	2 A

Fig. 7.   Voltage pulses for resistance and inductance identification. (a) Resistance identification. (b) Inductance identification.

Therefore

$$\Delta\theta = \sin^{-1}\left(\frac{D\omega_{\text{ref}} + T_L}{K_t I_{\max}}\right). \tag{34}$$

$\Delta\theta$ depends on the value of the steady-state load torque (T_L). This means that the dynamic characteristics given by (30) are also dependent on the steady-state value of the load torque. In practical implementations, (34) can be performed through a lookup table with ω_{ref} as an index. Moreover, stepper motors generally operate with $|\Delta\theta| < \pi/2$ to avoid step-out, so the validity of (31) is guaranteed.

VII. IMPLEMENTATION AND EXPERIMENTAL RESULTS

A. Implementation

A block diagram of the overall stepper motor control system is shown in Fig. 1, and a photograph of the corresponding hardware platform for the experiment with the proposed algorithms is shown in Fig. 6. The controller is based on one DSP TMSF2811, which handles all the motor parameter identification, the current control, the position control, and the damping algorithms. The controller is programmed and commanded by a standard PC through the joint test action group (JTAG) interface. In addition, the experimental system also contains a stepper motor and an optical encoder. The hybrid stepper motor, Fastech model EzM-56L, is a two-phase permanent stepper motor with 50 rotor teeth, giving a step angle of 1.8°. The motor is driven in microstepping algorithm with 1/50 step, resulting in a resolution of 10 000 steps per revolution (or pulses per revolution). This means that 1 revolution per second (rps) corresponds 10 000 pps. The optical encoder having 2500 lines or 10 000 pulses/rev is attached to the motor. The commanded voltages are supplied by a 40-kHz pulse width modulation (PWM) amplifier. The maximum output voltage of the PWM is ±40 V. The maximum current for the motor is 2 A. The parameters for the experimental system are shown in Table II. All of the parameter identifications, the current control, and the damping algorithms are executed at a rate of approximately 40 kHz. The speed is obtained using $\omega(kT_f) = [\theta(kT_f) - \theta((k-1)T_f)]/T_f$, with the fresh frequency T_f set to 1 kHz. At the beginning of the control program, the motor is maintained at standstill to identify

the resistances and inductances of the two coils of the motor. Two different voltage pulses are consequently commanded to the same coil of the motor. Specifically, the first voltage pulse shown in Fig. 7(a) with amplitude 1 V and width 20 ms is used to identify the resistance in the steady state of the phase current response. Similarly, to identify the inductance in the transient of the phase current response, the second voltage pulse shown in Fig. 7(b) with amplitude 40 V and width 200 μs is used. Moreover, to increase the accuracy of calibration for the analog–digital converter (ADC), two positive and negative voltage pulses are generated, as shown in Fig. 7, to produce the two corresponding positive and negative phase currents. After that, the average value given by (35) of the amplitudes of these phase currents is used for calculations in (8) and (9). The same scheme is applied to the other coil of the motor:

$$I = \frac{|I_+| + |I_-|}{2}. \tag{35}$$

After completely identifying the motor parameters, the motor drive is switched on to simultaneously execute current control, position control, and damping control programs.

B. Experimental Results

First, an experiment was performed to identify the stepper motor parameters. Second, the current controller was tested. Next, the position controller was tested. Finally, the damping method was tested.

1) Motor Parameter Identification: Table III shows the performance of the proposed identification technique. Compared to the nominal values given by the manufacturer, the average resistances of the phase A and the phase B of the motor are within 18.69% and 16.08%, respectively. Similarly, the average

TABLE III
MOTOR PARAMETER IDENTIFICATION RESULTS

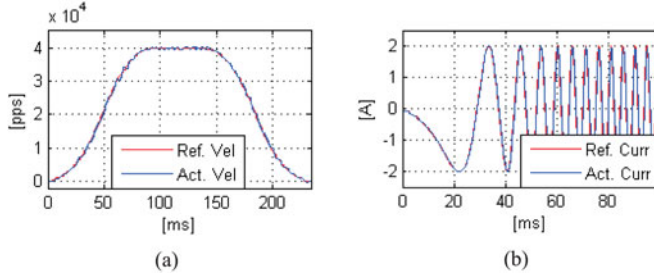| Parameter	Nominal	Phase A		Phase B	
		Estimate	Error	Estimate	Error
R	2.3 Ω	2.73 Ω	18.69%	2.67 Ω	16.08%
L	7.35 mH	6.59 mH	10.34%	6.37 mH	13.34%

Fig. 8. Motor speeds and phase currents with the conventional PI controller when the motor operates at 40 000 pps. (a) Reference and actual speeds. (b) Reference and actual currents.
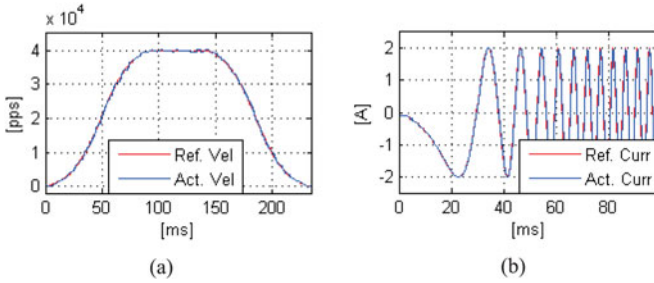
Fig. 9. Motor speeds and phase currents with the proposed PI controller when the motor operates at 40 000 pps. (a) Reference and actual speeds. (b) Reference and actual currents.

inductances of these two phases are within 10.34% and 13.34%, respectively. These average resistance and average inductance values are qualified for effectively designing the current controllers. They were later used in doing the next experiments for the current control and damping methods.

2) Current Controller: Next, we compare the proposed improved PI current controller of the phase B of the motor to the conventional PI current controller.

Figs. 8 and 9 show the motor speeds and currents when the motor is operated at 40 000 pps. The performances of the two current controllers are almost the same. The actual currents track the corresponding reference currents well, and all of the currents are shown in Figs. 8(b) and 9(b). The motor works normally at this speed, as shown in Figs. 8(a) and 9(a).

At a higher speed of 1 90 000 pps, the motor speeds and currents are shown in Figs. 10 and 11. With the conventional PI current controller, the stall problem shown in Fig. 10(a) occurs when the motor speed reaches to 1 30 000 pps, and the motor therefore does not work at this speed or higher. Moreover, as Fig. 10(b) shows, the actual current is not stable and is decreased in amplitude. In contrast, with the proposed improved PI current
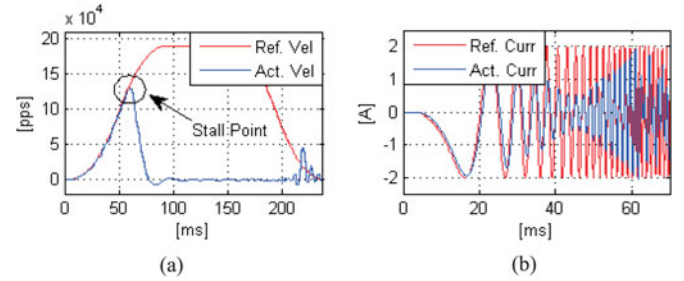
Fig. 10. Motor speeds and phase currents with the conventional PI controller when the motor operates at 1 90 000 pps. (a) Reference and actual speeds. (b) Reference and actual currents.
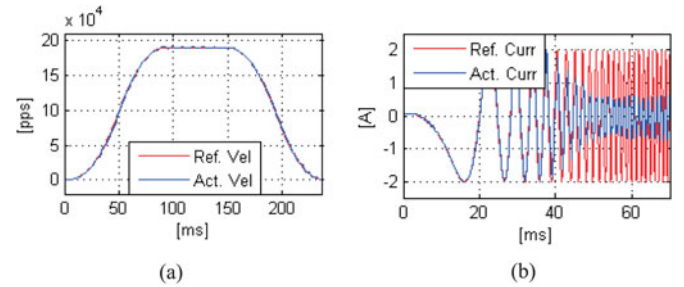
Fig. 11. Motor speeds and phase currents with the proposed PI controller when the motor operates at 1 90 000 pps. (a) Reference and actual speeds. (b) Reference and actual currents.

controller, as shown in Fig. 11(a), the stall problem is overcome and the motor runs easily over the stall point at 1 30 000 pps and then settles to the reference speed 1 90 000 pps. The current tracking performance and the stability, shown in Fig. 11(b), are better than those shown in Fig. 10(b) for the conventional PI current controller. However, the amplitude of the current still decreases from 2 to 0.5 A. This is normal when the stepper motor is operated at a high speed with microstepping of the current regulator without compensating for the back EMF.

Overall, with the adaptive capability of the proposed improved PI current controller to changes of the motor parameters and the operating speed, a good current characteristic is obtained. Furthermore, the bandwidth of the speed response is expanded, and the motor can work over a large operating speed range. However, the motor speed still oscillates strongly. This drawback is overcome by using the damping method presented later in this paper.

3) Position Controller: Next, the performance of the position controller is demonstrated. Fig. 12 shows the reference and actual speeds and the corresponding position error when a loss of synchronism in speed occurs. The motor operates normally until about 250 ms. At that moment, an external torque is applied to hold the rotor for 50 ms. This causes a loss of synchronism in motor speed. In addition, during this interval, the actual speed, shown in Fig. 12(a), decreases while the position error, shown in Fig. 12(b), increases to a very large value of 7900 pulses (close to one revolution). At a time of 300 ms, the external torque is removed, releasing the rotor to continue rotating. The actual speed increases to above the reference speed of 1 20 000 pps, reaching up to 1 50 000 pps. After that, the actual speed slows
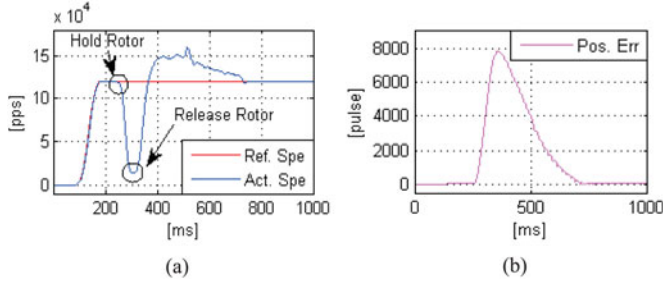
Fig. 12. Reference and actual speeds, and position error when there is a loss of synchronism. (a) Reference and actual speeds. (b) Position error.
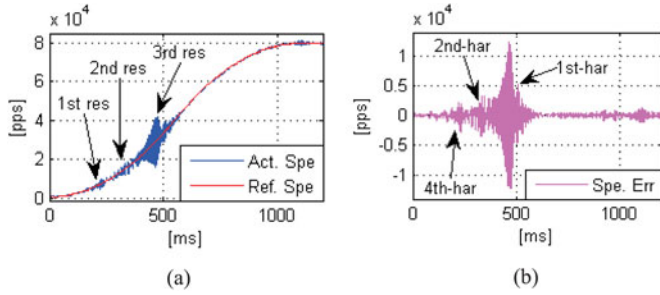

Fig. 13. Resonances when the motor is accelerated from 0 to 80 000 pps without damping. (a) Reference and actual speeds. (b) Speed error.

down and then tracks the reference speed at 720 ms. Thus, the position error is reduced to a very small value. Eventually, the synchronous condition in speed is recovered.

4) Damping Method: Finally, we compare the proposed damping method to the LA technique presented in [7]. The LA directly affects the motor torque, and is given by

$$\Delta\theta = \tan^{-1}\left(\frac{N_r \omega L}{R}\right) + \sin^{-1}\left(\frac{Zi_q}{V} + \frac{RN_r \omega \phi_m}{ZV}\right) \quad (36)$$

where $\Delta\theta$ is the LA [the same position error described in (25)], R and L are the identified motor parameters, $Z = \sqrt{R^2 + (N_r \omega L)^2}$ is the impedance of the winding of the motor, V is the supplied voltage to the motor, ϕ_m is the magnetic flux of the motor, and i_q is the q-axis current. All motor parameters are listed in Table II.

Here, i_q is calculated via Park's transformation as follows:

$$\begin{bmatrix} i_d \\ i_q \end{bmatrix} = \begin{bmatrix} \cos(\theta) & \sin(\theta) \\ -\sin(\theta) & \cos(\theta) \end{bmatrix} \times \begin{bmatrix} i_a \\ i_b \end{bmatrix}. \quad (37)$$

The first experiment demonstrates common resonance phenomena for the studied stepper motor. The reference speed, the actual speed, and the speed error are shown in Fig. 13 as the motor is accelerated from 0 to 80 000 pps in 1200 ms, in open-loop control and without damping. Fig. 13(a) clearly shows the actual resonances that occur at speeds of 7500, 15 000, and 30 000 pps, corresponding to driving currents at 0.75, 1.5, and 3 Hz, respectively. Fig. 13(b) shows the corresponding speed error, which reveals three corresponding harmonics. Among these harmonics, the oscillation at 3 Hz is the strongest.

Measuring the cycle time of each harmonic shows that these three harmonics oscillate with the mechanical natural frequency
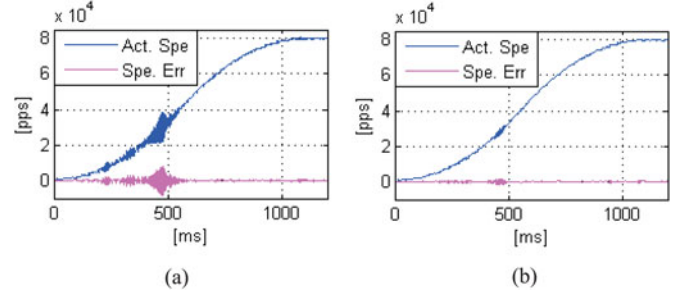

Fig. 14. Comparison between the lead-angle (LA) technique and the proposed damping method when the motor is accelerated from 0 to 80 000 pps. (a) Actual speed and speed error with the LA technique. (b) Actual speed and speed error with the proposed damping method.

of the motor ($f_n = 3.2$ Hz). The results also reveal that the 1st, 2nd, and 3rd resonances are caused by the 4th-, 2nd-, and 1st-harmonics, respectively (corresponding to $j = 4$, 2, and 1 in (5), respectively). In addition, Fig. 13(b) shows the maximum amplitude peak values of the harmonics, which are 2200, 3200, and 12 400 pps for the 4th-, 2nd-, and 1st-harmonics, respectively. These result in the corresponding amplitudes of (20) $K_{d4} \approx 0.0018$ N · m, $K_{d2} \approx 0.0026$ N · m, and $K_{d1} \approx 0.0101$ N · m, respectively.

Then, the optimal phase shift ϕ_j^* and the optimal amplitude K_{dj}^* are determined by using the procedure described in Step 2 of Subsection A of Section V. Specifically, $\phi_4^* = 2.618$ rad and $K_{d4}^* = 0.0012$ N · m for the 4th-harmonic; $\phi_2^* = 2.879$ rad and $K_{d2}^* = 0.002$ N · m for the 2nd-harmonic; and $\phi_1^* = 5.759$ rad and $K_{d1}^* = 0.012$ N · m for the 1st-harmonic.

The second experiment compares the performances of the motor speed between using the LA technique and using the proposed damping method when the motor is accelerated from 0 to 80 000 pps in 1200 ms. The reference speed is shown in Fig. 13(a), and the corresponding actual speeds and the speed errors are shown in Fig. 14. Specifically, Fig. 14(a) indicates the corresponding actual speed and the speed error with the LA technique. Three resonances still exist but are probably reduced compared to without damping. The actual speed and the speed error with the proposed damping method are shown in Fig. 14(b). The three resonances are completely removed, and the speed error is reduced to almost zero. This means that the proposed damping method significantly removes all the resonances.

The next experiments show the ability of the proposed damping method when the motor speed is steady and the motor operates over the full speed range, which is divided into four separate regions, as follows:

1) very low speed region: $\omega < 5000$ pps;
2) low-speed region: $5000 \text{ pps} \leq \omega < 80\,000$ pps;
3) medium-speed region: $80\,000 \text{ pps} \leq \omega < 2\,00\,000$ pps;
4) high-speed region: $\omega \geq 2\,00\,000$ pps.

    Case 1) The very low speed region: This speed region is below the resonant speeds. A speed of 4000 pps is selected for testing. Without damping, the actual speed oscillates quite strongly as can be seen in Fig. 15(a). The corresponding absolute maximum speed error is about 1000 pps, as shown in Fig. 15(b). The LA technique, shown in
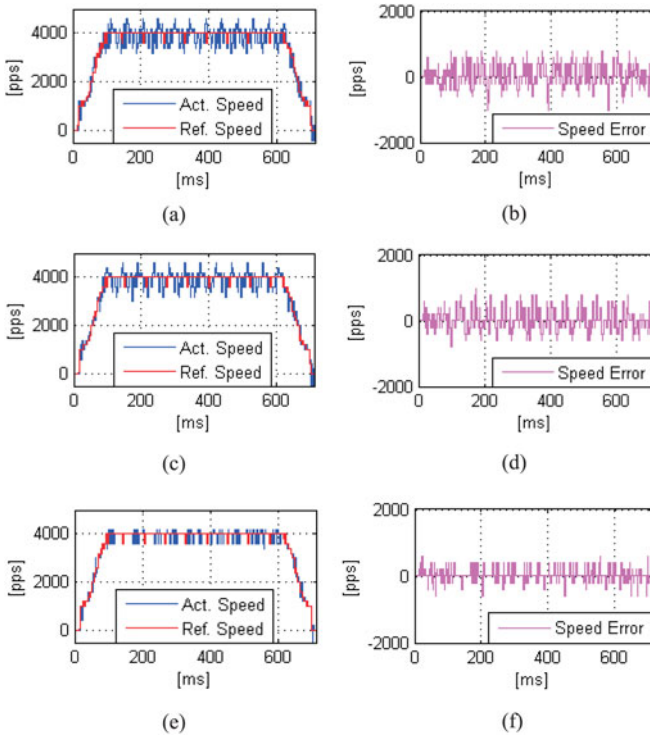
Fig. 15. Motor speeds and speed error at 4000 pps. (a)−(b) Without damping. (c)−(d) With the LA technique. (e)−(f) With the proposed damping method.
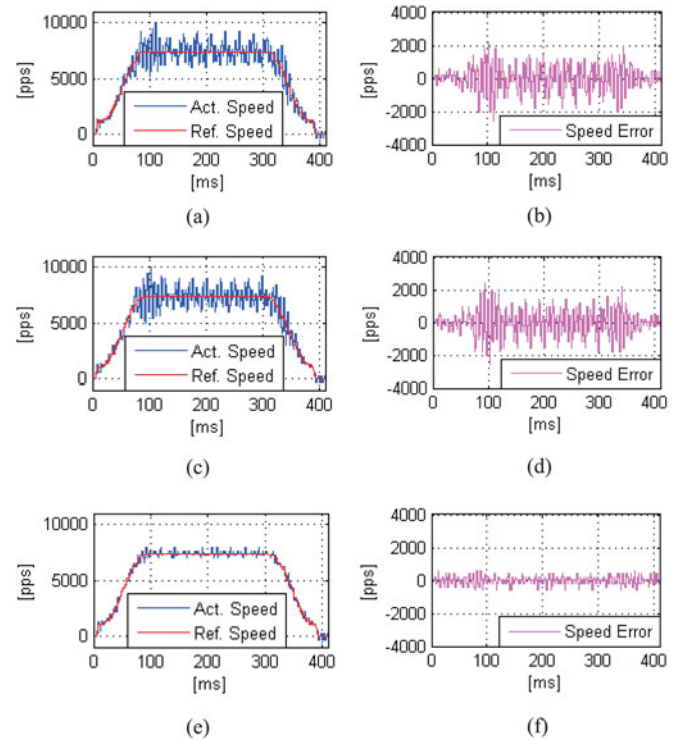

Fig. 16. Motor speeds and speed error at 7500 pps. (a)−(b) Without damping. (c)−(d) With the LA technique. (e)−(f) With the proposed damping method.

Fig. 15(c) and (d), seems not to affect the motor speed performance at this speed. The absolute maximum speed error, shown in Fig. 15(d), is the same value 1000 pps compared to without damping. Fig. 15(e) and (f) shows the performance with the proposed damping method. The oscillations are significantly reduced, and the absolute maximum speed error is decreased to 500 pps, shown in Fig. 15(f). Overall, the proposed damping method achieves the best speed performance at this speed region.

Case 2) The low-speed region: Three resonances occur in this speed region. Figs. 16− 18 show the motor speeds and the speed errors at the three different resonant speeds in three different cases without damping, with the LA technique, and with the proposed damping method.

Without damping, because 7500, 15 000, and 30 000 pps are mostly near the middle of the resonance regions, the oscillations of the motor are rather large, as shown in Figs. 16(a)–18(a), respectively. The corresponding absolute maximum speed errors are 2000 pps [Fig. 16(b)], 3000 pps [Fig. 17(b)], and 10 000 pps [Fig. 18(b)], respectively.

In contrast, at these three speeds, the LA technique is rather effective at the speed 30 000 pps [Fig. 18(c)] with the absolute maximum speed error 6000 pps [Fig. 18(d)], is acceptable at 15 000 pps [Fig. 17(c)] with the absolute maximum speed error 2500 pps [Fig. 17(d)], and seems not to affect the motor speed performance at 7500 pps [Fig. 16(c)] with the absolute maximum speed error 2000 pps [Fig. 16(d)].
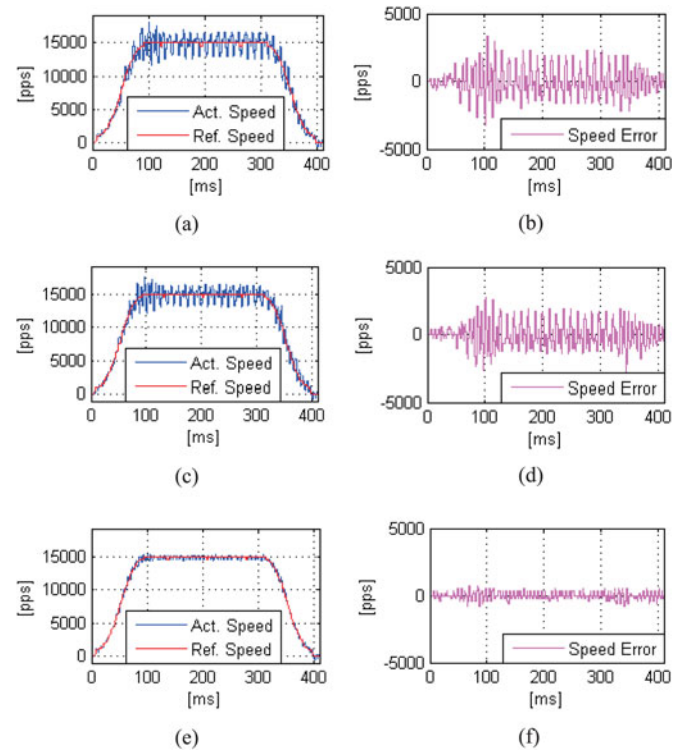

Fig. 17. Motor speeds and speed error at 15 000 pps. (a)−(b) Without damping. (c)−(d) With the LA technique. (e)−(f) With the proposed damping method.
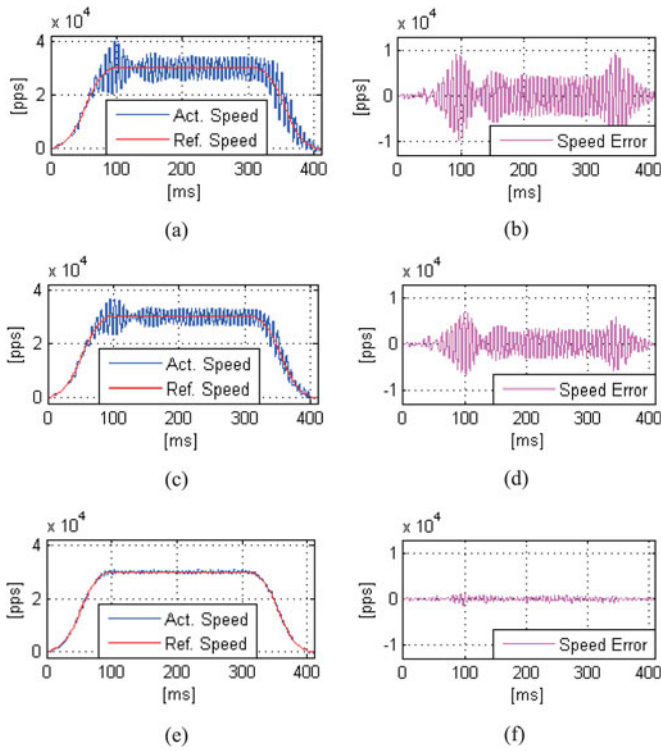
Fig. 18. Motor speeds and speed error at 30 000 pps. (a)−(b) Without damping. (c)−(d) With the LA technique. (e)−(f) With the proposed damping method.

Fig. 19. Motor speeds and speed error at 1 20 000 pps. (a)−(b) Without damping. (c)−(d) With the LA technique. (e)−(f) With the proposed damping method.

Furthermore, the proposed damping method shown in Figs. 16(e−f)–18(e−f) works perfectly because it significantly removes all resonances. Particularly, at the speed 7500 pps, the value of the absolute maximum speed error is 500 pps with the proposed damping method, which is shown in Fig. 16(f). This value is the smallest compared to 2,000 pps with the LA technique [Fig. 16(d)], and it becomes 2,000 pps without damping [Fig. 16(b)]. At the higher speed 15 000 pps, comparing to the value 2500 pps with the LA technique [Fig. 17(d)], and 3000 pps without damping [Fig. 17(b)], the value 800 pps [Fig. 17(f)] with the proposed damping method is the smallest value. The proposed damping method achieves the best performance compared to the LA technique and without damping, at the speed 30 000 pps. The absolute maximum speed error is a small value of 1000 pps [Fig. 18(f) compared to a medium value of 6000 pps with the LA technique (Fig. 18(d)), and a large value of 10 000 pps without damping [Fig. 18(b)]. Obviously, the proposed damping method is better than the LA technique in this speed region.

Case 3) The medium-speed region: The testing speed of 1 20 000 pps represents the medium-speed region. The speed performances are shown in Fig. 19. The vibration of the actual speed without damping, shown in Fig. 19(a), is quite large. The corresponding absolute maximum speed error is about 6500 pps, which is large and is shown in Fig. 19(b). The actual speed responses with the LA technique, shown in Fig. 19(c), and with the proposed damping method, show in Fig. 19(e), are almost the same. They both significantly suppress the vibrations in the constant
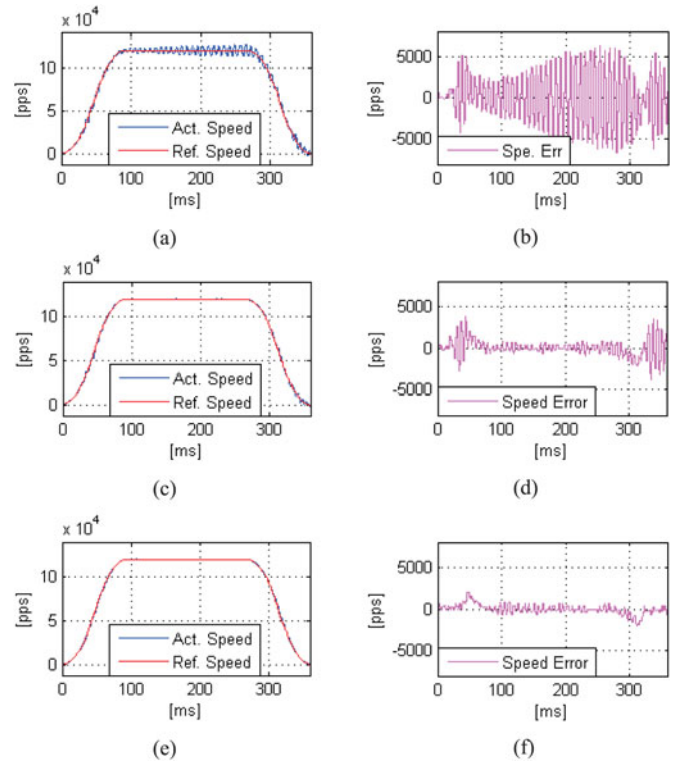
speed interval with the same absolute maximum speed error about 800 pps, as shown in Fig. 19(d) and (f). However, in the acceleration and deceleration intervals, especially in the low-speed region where the resonances occur, the proposed damping method is considerably better than the LA technique. The corresponding absolute maximum speed error is 2000 pps with the proposed damping method, shown in Fig. 19(f), compared to 3900 pps with the LA technique, shown in Fig. 19(d). Moreover, with the proposed damping method, the motor is stopped more stably compared to the LA technique.

Case 4) The high-speed region: The system is tested at a speed of 2 70 000 pps, which represents the high-speed region. The comparison between without damping, with the LA technique, and with the proposed damping method at this speed is shown in Fig. 20. The same explanation is given as for the speed of 1 20 000 pps discussed earlier. Without damping, the motor vibrates strongly and is shown in Fig. 20(a). In contrast, both the LA technique and the proposed damping method perfectly suppress the vibrations, as shown in Fig. 20(c) and (e), respectively. Particularly, in the constant speed interval, the absolute maximum speed errors are the same 700 pps, shown in Fig. 20(d) and (f), compared to a large value of 7000 pps without damping, shown in Fig. 20(b). The proposed damping method makes the motor operate more smoothly than the LA technique in the start-point and stop-point vicinities, shown in Fig. 20(d) and (f). The absolute maximum speed error with the proposed damping method
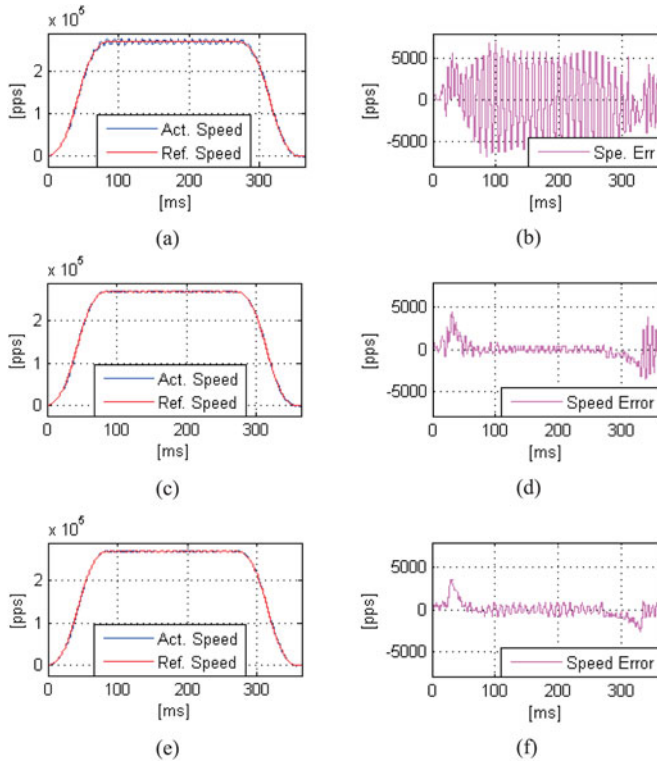
Fig. 20.   Motor speeds and speed error at 2 70 000 pps. (a)−(b) Without damping. (c)−(d) With the LA technique. (e)−(f) With the proposed damping method.

VIII.   CONCLUSION

We have proposed a control approach to improve the performance of the stepper motor. The motor operates at high speed. The high torque is generated to avoid step-out, and the synchronism in speed is guaranteed. In addition, the motor operates smoothly over the whole speed range. The speed performance with the proposed damping method is probably better than that with the LA technique, especially in low- and very low speed regions. All the proposed algorithms are simple, reliable, and effective; they do not require any transformation; and they are performed within only one stationary frame.

Because the experiments were obtained on a DSP-based industrial setup, the results have a clear potential application to industrial processes for improving performance and efficiency. However, the damping scheme requires an identification procedure for resonances. Moreover, this damping method is limited to applications with varying loads. In the future, it may be feasible to upgrade the stepper motor control system by considering online resonance identification techniques to adapt to varying loads.

TABLE IV

COMPARISON OF DAMPING PERFORMANCE BETWEEN WITHOUT DAMPING, WITH THE LA TECHNIQUE, AND WITH THE PROPOSED DAMPING METHOD

Speed [pps]	Absolute Maximum Speed Error [pps]				
	Without	LA Technique		Proposed Method	
		Constant	Acc–Dec	Constant	Acc–Dec
4000	1000	1000	—	500	—
7500	2000	2000	—	500	—
15 000	3000	2500	—	800	—
30 000	10 000	6000	—	1000	—
1 20 000	6500	800	3900	800	2000
2 70 000	7000	700	4300	700	3500

is 3500 pps, as shown in Fig. 20(f), compared to 4300 pps with the LA technique, shown in Fig. 20(d).

To summarize briefly the damping performances in all four aforementioned cases, the absolute maximum speed errors in the constant speed interval and in the acceleration–deceleration interval are shown in Table IV. Overall, compared to the LA technique, the proposed damping method is significantly better in very low- and low-speed regions. In medium- and high-speed regions, the two methods have almost the same performance in the constant speed interval, but the proposed damping method is better than the LA technique in the acceleration and deceleration intervals.

REFERENCES

[1] S. Derammelaere *et al.*, "The efficiency of hybrid stepping motors: Analyzing the impact of control algorithms," *IEEE Ind. Appl. Magaz.*, vol. 20, no. 4, pp. 50–60, Jul./Aug.2014.

[2] Y. I. Son, I. H. Kim, D. S. Choi, and H. Shim, "Robust cascade control of electric motor drives using dual reduced-order PI observer," *IEEE Trans. Ind. Electron.*, vol. 62, no. 6, pp. 3672–3682, Jun. 2015.

[3] M. Marufuzzaman, M. B. I. Reaz, and M. A. M. Ali, "FPGA implementation of an intelligent current dq PI controller for FOC PMSM drive," in *Proc. IEEE Comput. Appl. Ind. Electron.*, 2010, pp. 602–605.

[4] J. W. Jung, Y. S. Choi, V. Q. Leu, and H. H. Choi, "Fuzzy PI-type current controllers for permanent magnet synchronous motors," *IET Electr. Power Appl.*, vol. 5, no. 1, pp. 143–152, 2011.

[5] P. Crnosija, B. Kuzmanovic, and S. Ajdukovic, "Microcomputer implementation of optimal algorithms for closed-loop control of hybrid stepper motor drives," *IEEE Trans. Ind. Electron.*, vol. 47, no. 6, pp. 1319–1325, Dec. 2000.

[6] A. Hoda and K. Abe, "Control apparatus for position control motor," U.S. Patent 6 121 744, Septembers 19, 2000.

[7] A. Takemori, Y. Kuwano, Y. Takahashi, and H. Taka, "Stepping motor driver," U.S. Patent 6 850 026, February 1, 2005.

[8] S. A. Schweid, J. E. McInroy, and R. M. Lofthus, "Closed loop low velocity regulation of hybrid stepping motors amidst torque disturbances," *IEEE Trans. Ind. Electron.*, vol. 42, no. 3, pp. 316–324, Jun. 1995.

[9] Y. Lee, D. Shin, W. Kim, and C. C. Chung, "Proximate in-phase current estimator to reduce torque ripple in permanent-magnet stepping motor," *IEEE Trans. Ind. Electron.*, vol. 63, no. 3, pp. 1707–1716, Mar. 2016.

[10] S. M. Yang and E. L. Kuo, "Damping a hybrid stepping motor with estimated position and velocity," *IEEE Trans. Power Electron.*, vol. 18, no. 3, pp. 880–887, May 2003.

[11] J. Hirai, T. W. Kim, and A. Kawamura, "Position-sensorless drive of linear pulse motor for suppressing transient vibration," *IEEE Trans. Ind. Electron.*, vol. 47, no. 2, pp. 337–345, Apr. 2000.

[12] H. Melkote and F. Khorrami, "Robust nonlinear control and torque ripple reduction for permanent magnet stepper motors," *IEE Proc. Control Theory Appl.*, vol. 146, no. 2, pp. 186–196, Mar. 1999.

[13] T. Su, M. Ishida, and T. Hori, "Suppression control method for torque vibration of three-phase HB-type stepping motor utilizing feedforward control," *IEEE Trans. Ind. Electron.*, vol. 49, no. 4, pp. 896–904, Aug. 2002.

[14] T. Miura and T. Taniguchi, "Rotor oscillation damping of a stepping motor by sliding mode control," *IEEE Trans. Ind. Appl.*, vol. 117D-, no. 11, pp. 1375–1383, Nov. 1997.

[15] W. D. Chen, K. L. Yung, and K. W. Cheng, "Profile tracking performance of a low ripple hybrid stepping motor servo drive," *IEE Proc. Control Theory Appl.*, vol. 150, no. 1, pp. 69–76, Jan. 2003.

[16] K. W. Tsui, N. C. Cheung, and K. C. Yuen, "Novel modeling and damping technique for hybrid stepper motor," *IEEE Trans. Ind. Electron.*, vol. 56, no. 1, pp. 202–211, Jan. 2009.

[17] T. S. Hwang, J. K. Seok, and D. H. Kim, "Active damping control of linear hybrid stepping motor for cogging force compensation," *IEEE Trans. Magn.*, vol. 42, no. 2, pp. 329–334, Feb. 2006.

[18] T. S. Hwang and J. K. Seok, "Observer-based ripple force compensation for linear hybrid stepping motor drives," *IEEE Trans. Ind. Electron.*, vol. 54, no. 5, pp. 2417–2424, Oct. 2007.

[19] S. M. Yang, F. C. Lin, and M. T. Chen, "Micro-stepping control of a two-phase linear stepping motor with three-phase VSI inverter for high speed applications," *IEEE Trans. Ind. Appl.*, vol. 40, no. 5, pp. 1257–1264, Sep./Oct. 2004.

[20] T. Miura and T. Taniguchi, "Open-loop control of a stepping motor using oscillation-suppressive exciting sequence tuned by genetic algorithm," *IEEE Trans. Ind. Electron.*, vol. 46, no. 6, pp. 1192–1198, Dec. 1999.

[21] W. D. Chen, K. L. Yung, and K. W. Cheng, "A learning scheme for low speed precision tracking control of hybrid stepping motors," *IEEE/ASME Trans. Mechatronics*, vol. 11, no. 3, pp. 362–365, Jun. 2006.

[22] F. Betin, D. Pinchon, and G. A. Gapolino, "Fuzzy logic applied to speed control of a stepping motor drive," *IEEE Trans. Ind. Electron.*, vol. 47, no. 3, pp. 610–622, Dec. 2000.

[23] Q. N. Le and J. W. Jeon, "Neural-network-based low-speed-damping controller for stepper motor with an FPGA," *IEEE Trans. Ind. Electron.*, vol. 57, no. 9, pp. 3167–3180, Sep. 2010.

[24] G. Wang, R. Yang, and D. Xu, "DSP-based control of sensorless IPMSM drives for wide-speed-range operation," *IEEE Trans. Ind. Electron.*, vol. 60, no. 2, pp. 720–727, Feb. 2013.

[25] S. Derammelaere *et al.*, "Load angle estimation for two-phase hybrid stepping motors," *IET Electric Power Appl.*, vol. 8, no. 7, pp. 257–266, Aug. 2014.

[26] N. Matsui, M. Nakamura, and T. Kosaka, "Instantaneous torque analysis of hybrid stepping motor," *IEEE Trans. Ind. Appl.*, vol. 32, no. 5, pp. 1176–1182, Sep./Oct. 1996.

[27] P. Acarnley, *Stepping Motors: A Guide to Theory and Practice*. London, U.K.: The Institution of Engineering and Technology, 2007, Ch. 4.

Hung Van Hoang received the B.S. degree in electrical and electronics engineering from Ho Chi Minh City University of Technology, Ho Chi Minh City, Vietnam, in 2003, and the M.S. and Ph.D. degrees in electrical and computer engineering from Sungkyunkwan University, Suwon, South Korea, in 2008 and 2011, respectively.

From 2011 to 2013, he was a Postdoctoral Researcher with the School of Information and Communication Engineering, Sungkyunkwan University, South Korea. He is currently a Senior Researcher with Fastech Company Ltd., Gyeonggi, South Korea. His research interests include motion control, embedded systems, and real-time applications.

Jae Wook Jeon (S'82–M'84) received the B.S. and M.S. degrees in electronics engineering from Seoul National University, Seoul, South Korea, in 1984 and 1986, respectively, and the Ph.D. degree in electrical engineering from Purdue University, West Lafayette, IN, USA, in 1990.

From 1990 to 1994, he was a Senior Researcher with Samsung Electronics, Suwon, South Korea. In 1994, he was an Assistant Professor with the School of Information and Computer Engineering, Sungkyunkwan University, Suwon, where he is currently a Professor. His research interests include robotics, embedded systems, and factory automation.

Kien Minh Le received the B.S. degree in electrical engineering from Hanoi University of Technology, Hanoi, Vietnam, in 2006, and the M.S. degree in automation from Le Quy Don Technical University, Hanoi, Vietnam, in 2011. He is currently working toward the Ph.D. degree in the School of Information and Communication Engineering, Sungkyunkwan University, Suwon, South Korea.

His research interests include motion control and embedded systems.